# A Charge Transfer Model for CMOS Image Sensors

Liqiang Han, *Student Member, IEEE*, Suying Yao, *Member, IEEE*, and Albert J. P. Theuwissen, *Fellow, IEEE*

***Abstract*— Based on the thermionic emission theory, a charge transfer model has been developed which describes the charge transfer process between a pinned photodiode and floating diffusion (FD) node for CMOS image sensors. To simulate the model, an iterative method is used. The model shows that the charge transfer time, barrier height, and reset voltage of the FD node affect the charge transfer process. The corresponding measurement results obtained from two different test chips are presented in this paper. The model also predicts that other physical parameters, such as the capacitance of the FD node and the area of the photodiode, will affect the charge transfer. Furthermore, the model can be extended to explain the pinning voltage measurement method and the feedforward effect.**

***Index Terms*— CMOS image sensors (CISs), pinned photodiode (PPD), thermionic emission theory.**

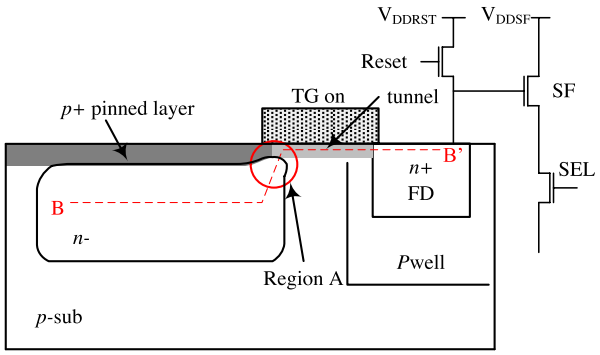


Fig. 1. 4T pixel architecture.

## I. Introduction

CMOS image sensors (CISs) are widely used nowadays in the fields of electronic imaging, such as consumer, scientific, and military applications. The pinned photodiode (PPD) is the most important component in a CIS. The implants of the PPD and the transfer gate (TG) must be accurately controlled and optimized for the purpose of low image lag, low dark current, and large full well capacity (FWC) [1]–[3]. Small implant adjustments in implant energy, dose, tilt, and mask position will affect the performance dramatically [4], [5]. It is popular to utilize TCAD tools to study the performance of a CIS [6]–[8]. However, implant adjustments are still required in actual manufacturing.

Since the doping profile under the TG is so complicated, it is difficult to describe the charge transfer process using a drift diffusion (DD) model without TCAD tools. Self-induced drift, thermal diffusion, and fringing field effects are common views for charge transfer in charge coupled devices (CCD) [9]. A similar viewpoint for CIS can be found in [10]. In standard 4T CIS pixels, the PPD and floating diffusion (FD) node are separated, which is very different from a CCD where the electrodes are adjacent. For the PPD structure, the subthreshold current is used to explain the charge transfer with a small signal level [11]. In [12], subthreshold current, also called emission current, is used to explain charge transfer noise and image lag. The emission current originates from the thermal motion phenomenon of electrons, where the electrons which have enough thermal velocity in the transfer direction will cross the barrier on the charge transfer path [13]. In [6], [14], and [15], methods are shown for the ideal charge transfer path without a barrier, which needs a very precise doping control. In actual manufacturing, both the increased surface boron implant dose for sufficient surface pinning and dark current reduction, and the out-diffusion phenomena of boron itself may result in a barrier on the charge transfer path [16], which affects the charge transfer efficiency dramatically.

In standard 4T pixels, the typical charge transfer time is 1 $\mu s$. For some high speed applications, the charge transfer time should be much shorter, e.g., 40 ns [17]. In many papers, see [5], [18], [19], a nonlinear photoresponse with low exposure levels is observed if the charge transfer time is not long enough. This leads to a low charge transfer efficiency and may result in serious image lag.

In this paper, we establish a charge transfer model to describe the charge transfer process between the PPD and the FD node based on the thermionic emission theory. Section II describes the model in detail. Section III shows some measurement results corresponding to the model prediction. Section IV gives two examples of the model extension. Finally, the conclusion is drawn in Section V.

## II. Charge Transfer Model in a CIS

A typical 4T pixel is shown in Fig. 1. The BB′ is the charge transfer path when a high voltage is applied to the TG. Several implants, at least including $p+$ for the pinned layer and $n-$ for the PPD, affect the potential distribution in region A, where a

Manuscript received March 20, 2015; revised June 13, 2015; accepted June 23, 2015. Date of publication July 28, 2015; date of current version December 24, 2015. The review of this paper was arranged by Editor J. R. Tower.

L. Han is with the School of Electronic Information Engineering, Tianjin University, Tianjin 300072, China, and also with the Electronic Instrumentation Laboratory, Delft University of Technology, Delft 2628CD, The Netherlands (e-mail: h.liqiang@tudelft.nl and hlq@tju.edu.cn).

S. Yao is with the School of Electronic Information Engineering, Tianjin University, Tianjin 300072, China (e-mail: syyao@tju.edu.cn).

A. J. P. Theuwissen is with Harvest Imaging, Bree 3960, Belgium, and also with the Electronic Instrumentation Laboratory, Delft University of Technology, Delft 2628CD, The Netherlands (e-mail: a.j.p.theuwissen@tudelft.nl).

Color versions of one or more of the figures in this paper are available online at http://ieeexplore.ieee.org.

Digital Object Identifier 10.1109/TED.2015.2451593

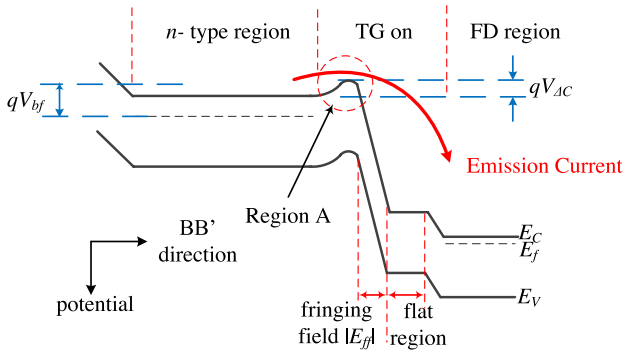


Fig. 2. Potential diagram along BB′.

barrier may occur. Because of this potential barrier, we have developed a charge transfer model based on the thermionic emission theory in Section II-A. In Section II-B, we prove that this emission theory-based model is also applicable for pixels without barriers. In Sections II-C and II-D, the effect of conduction band variation and the FD potential is considered, respectively.

### *A. Level-1 Model: Thermionic Emission Theory in Pixel*

Fig. 2 shows the potential diagram along the cross section of BB′ when the TG is open, where $E_C$, $E_f$, and $E_V$ represent the energy levels of the conduction band, Fermi level, and valence band, respectively; $q$ is the electron charge; $qV_{\Delta C}$ is the barrier height on the charge transfer path; $qV_{\rm bf}$ is the difference between the conduction band barrier in region A and the Fermi level in the $n-$ PPD region; and $|E_{\rm ff}|$ is the fringing field intensity. In this paper, the electrostatic potential in a semiconductor is defined as the potential of the middle of the bandgap.

There are six assumptions for this level-1 model.

1) $qV_{\rm bf}$ is much larger than $kT$, where $k$ is the Boltzmann constant, and $T$ is the absolute temperature.
2) Region A and the fringing field region are fully depleted.
3) The conduction band is fixed.
4) $|E_{\rm ff}|$ is large enough, and the electrons will quickly drift to the FD node if they can cross the barrier. The total current flow is limited by the emission current.
5) During the charge transfer phase, the Fermi level in the $n-$ region is balanced, and the charge transfer process in the PPD is neglected. This is suitable for pixels with a small PPD area and large pixels with a special design for a built-in electric field [1], [8], [17], [20].
6) The number of transferred electrons is small and the potential of the FD node is high enough so that the effect of the electrons in the flat region of the tunnel as shown in Fig. 2 is neglected, and the charge transfer process is unidirectional.

The emission current from the PPD to the FD node is written as follows:

$$I_{\rm PPD-FD} = dQ/dt = I_0 \exp(-qV_{\rm bf}/kT) \tag{1}$$

$$I_0 = A \cdot S_A \cdot T^2 \tag{2}$$

where $A$ is the Richardson constant [13], and $S_A$ is the area of the cross section on the charge transfer path at the barrier position.

The number of electrons in the PPD $N_e$ can be obtained by the famous equation

$$N_e/V = n_e = N_C \exp(q(V_{\Delta C} - V_{\rm bf})/kT) \tag{3}$$

where $V$ is the volume of the PPD, $n_e$ is the electron density, and $N_C$ is the conduction band effective density of states. From (3), we can obtain

$$V_{\rm bf} = V_{\Delta C} - kT/q \times \ln\left(N_e/N_C V\right). \tag{4}$$

Substituting (4) with (1), and using $dQ = -qdN_e$

$$-N_e^{-1} dN_e = I_0/\left(qN_C V\right) \times \exp\left(-qV_{\Delta C}/kT\right) dt \tag{5}$$

$$-\int_{N_{e0}}^{N_e} N_e^{-1} dN_e = I_0/\left(qN_C V\right) \int_0^t \exp\left(-qV_{\Delta C}/kT\right) dt \tag{6}$$

where $N_{e0}$ is the initial number of electrons in the PPD, and $t$ is the charge transfer time. Then, we can obtain

$$N_e = N_{e0} \exp\left(-\frac{I_0}{qN_C V} \exp\left(-\frac{qV_{\Delta C}}{kT}\right) t\right) \tag{7}$$

where $N_e$ also represents the number of residual electrons after the charge transfer phase. Therefore, the number of transferred electrons from the PPD to the FD node in the given transfer time is

$$N_{\rm transfer} = N_{e0}\left[1 - \exp\left(-\frac{I_0}{qN_C V} \exp\left(-\frac{qV_{\Delta C}}{kT}\right) \times t\right)\right]. \tag{8}$$

Equation (8) is the level-1 charge transfer model. The relationship between $N_{\rm transfer}$ and $N_{e0}$ is linear for a given $t$.

Fig. 3(a) shows an example of the photoresponse curve based on the level-1 model, where $N_{e0}$ and $N_{\rm transfer}$ correspond to the exposure and output, respectively. If $t$ is long enough, the exponential term in (8) approximates to zero, and the charge transfer is complete. With a certain $N_{e0}$ as shown in Fig. 3(b), the relationship between $N_{\rm transfer}$ and $t$ is exponential, and the charge transfer process is mainly completed during the beginning of the charge transfer phase.

### *B. Supplement for the Level-1 Model: Diffusion Theory*

As mentioned in Section I, it is hard to say that all pixels have a potential barrier on the transfer path, even though a monotonic potential distribution is difficult to implement. For those pixels which have an ideal transfer path as shown in Fig. 4, the emission theory is also applicable. A simple derivation is given below.

The emission theory is established by calculating the number of electrons that have enough thermal velocity in the transfer direction to cross the barrier per time unit. The thermal motion phenomenon of a particle is the physical basis. For a typical PPD structure, the order of magnitude of the $n-$ region doping concentration is $10^{15}$–$10^{16}$ cm$^{-3}$, which means that assumption 1) in the level-1 model is also valid. Thus, the derivation of the emission current which is based

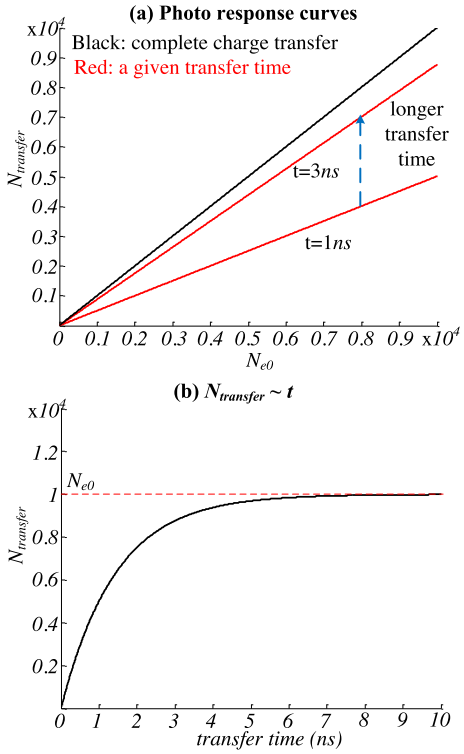


Fig. 3. Photoresponse in the level-1 model. (a) $N_{\text{transfer}}$ versus $N_{e0}$ and (b) $N_{\text{transfer}}$ versus $t$, where $T = 300$ K, $N_{e0} = 10000$, $qV_{\Delta C} = 0.05$ eV, $A = 120$ A/T$^2$cm$^2$, $S_A = 0.4$ $\mu$m$^2$, and $V = 8$ $\mu$m$^2$.

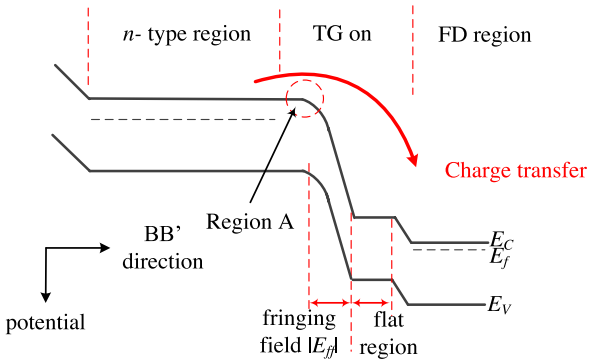


Fig. 4. Charge transfer path without a barrier.

on the Boltzmann distribution is applicable for this condition. Without a barrier, (1) can be written as

$$I = \left(4\pi q m^* k^2/h^3\right) \cdot T^2 \exp((qE_{C\text{fn}} - qE_{C\text{n}})/kT) \quad (9)$$

where $4\pi qm^*k^2/h^3$ is the extended form of the Richardson constant $A$, $h$ is the Planck constant, $m^*$ is the effective mass of the electron, and $E_{C\text{fn}}$ and $E_{C\text{n}}$ are the Fermi level and conduction band in the $n-$ region, respectively. Substituting $N_C = 2(2\pi m^* kT)^{3/2}/h^3$ with (9), we can achieve

$$I = q(kT/2\pi m^*)^{1/2} N_C \exp((qE_{C\text{fn}} - qE_{C\text{n}})/kT) \quad (10)$$

$$I = q(kT/2\pi m^*)^{1/2} n_e. \quad (11)$$

We call (11) the degraded emission current.

Assume there is a piece of semiconductor with a charge density gradient in the $x$-axis direction as shown in Fig. 5,

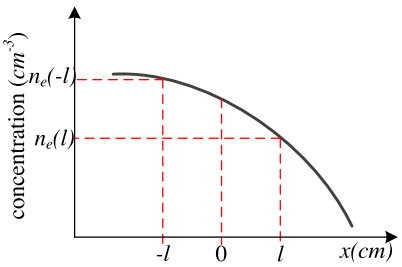


Fig. 5. Gradient concentration.

where $n_e(l)$ and $n_e(-l)$ are the charge density at $x = l$ and $x = -l$, respectively. Using the degraded emission theory, the current at $x = 0$ due to electrons that originate at $x = -l$ and move from left to right is

$$I_{r\to l} = -q \times n_e(-l) \times (kT/2\pi m^*)^{1/2}. \quad (12)$$

The current at $x = 0$ due to charges that originate at $x = l$ and move from right to left is

$$I_{l\to r} = -q \times n_e(l) \times (kT/2\pi m^*)^{1/2}. \quad (13)$$

Then, the total current at $x = 0$ is

$$I_{x=0} = I_{r\to l} - I_{l\to r} = q(kT/2\pi m^*)^{1/2} \times (n_e(l) - n_e(-l)). \quad (14)$$

It should be noted that the collision effect is neglected in the thermionic emission theory. Therefore, we consider $l$ in (14) to be equal to the mean free path

$$I_{x=0} = q(kT/2\pi m^*)^{1/2} \times 2l \frac{(n_e(l) - n_e(-l))}{2l} \quad (15)$$

$$I_{x=0} = ql(2kT/\pi m^*)^{1/2} \frac{dn_e(x)}{dx} \quad (16)$$

where $(2kT/\pi m^*)^{1/2}$ is equal to the thermal velocity $v_{\text{th}}$, which is well known as the mean of the magnitude of the velocity in any one dimension. Equation (16) can be written as

$$I_{x=0} = ql v_{\text{th}} \frac{dn_e(x)}{dx} = qD_n \frac{dn_e(x)}{dx} \quad (17)$$

where $lv_{\text{th}}$ is equal to the diffusion constant $D_n$ [21]. This is the thermal diffusion theory.

From (12)–(17), we know that the diffusion theory is bidirectional. However, the degraded emission current is unidirectional, which means an external force is needed to keep this unidirectional transfer, otherwise the transfer will become bidirectional again. We consider assumption 4) in the level-1 model to be valid for well-designed pixels. For example, the band bending in the fringing field region is 1 eV at a depth (width) of 0.15 $\mu$m with a linear distribution, where $|E_{\text{ff}}|$ is ~66 667 V/cm. As a result, $\mu|E_{\text{ff}}|$ is much larger than $v_{\text{th}}$, where $\mu$ is the electron mobility. The charge transfer is limited by the current flow in region A.

In conclusion, both the diffusion theory and emission theory originate from the thermal motion of electrons. For pixels with an ideal charge transfer path, the degraded emission current and diffusion current originate from the same physical process in region A. We use this degraded emission theory instead

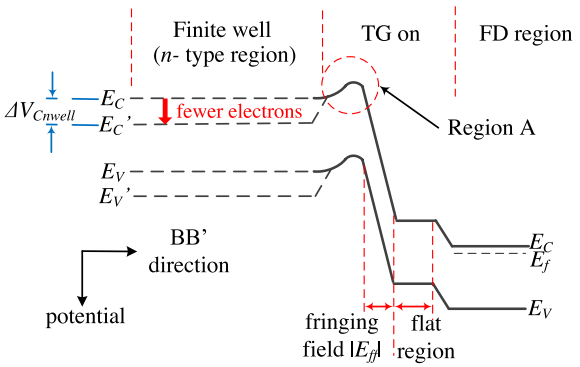


Fig. 6. Conduction band correction.

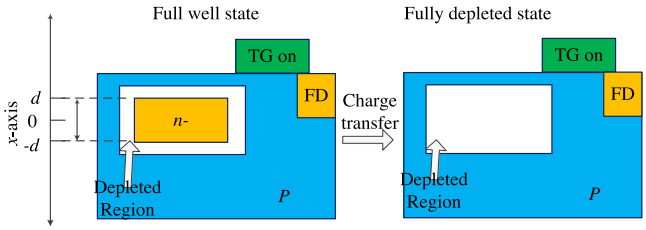


Fig. 7. PPD structure with a uniform doping concentration.

of DD model in region A, so that the level-1 model is also applicable because of the existence of $|E_{\text{ff}}|$.

### C. Level-2 Model: Conduction Band Correction

The PPD is a finite well for electrons which is fully depleted after a complete charge transfer. As the number of electrons in the PPD decreases, there are more fixed positive charges which lead to a stronger electrical field from the inside of the PPD to region A. Therefore, the effect of conduction band variation is considered in the level-2 model. Assumption 3) in the level-1 model should be modified as follows: the conduction band profile in region A should be fixed under a certain voltage applied to the TG, but the conduction band inside the PPD varies with the number of electrons as shown in Fig. 6.

We expect to obtain the following corrected equation for the conduction band potential:

$$V_{\Delta C} = V_{\Delta C0} + \Delta V_{C\text{nwell}} \tag{18}$$

where $\Delta V_{C\text{nwell}}$ reflects the variation of the conduction band potential in the $n-$ region, and $V_{\Delta C0}$ is defined as the barrier height when the number of electrons in the PPD is equal to the FWC with a certain high voltage applied to the TG.

As shown in Fig. 7, we assume that the doping concentration is uniform. The $x$-axis represents the depth direction, the depth of the undepleted PPD region is $2d$ under full well condition for a horizontal PPD structure. Solving the Poisson equation to get the relationship between the $N_e$ and $\Delta V_{C\text{nwell}}$

$$d^2\varphi_C/dx^2 = -q\left(N_D + n_e\right)/\varepsilon \tag{19}$$

where $N_D$ is the doping concentration of the $n-$ region, $\varepsilon$ is the permittivity of silicon, and $\varphi_C$ is the conduction band

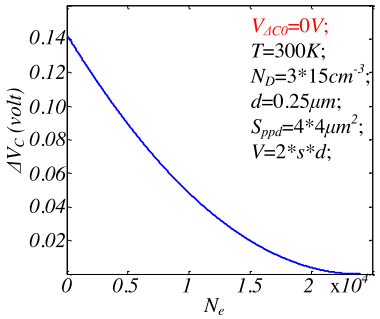


Fig. 8. Example of conduction band potential variation.

potential. Multiplying both sides by $d\varphi_C$ gives

$$\frac{d\left(d\varphi_C/dx\right)}{dx}d\varphi_C = -\frac{q}{\varepsilon}\left(N_D + n_e\right)d\varphi_C \tag{20}$$

$$\int_0^{d\varphi_C/dx}\frac{d\varphi_C}{dx}d\left(\frac{d\varphi_C}{dx}\right) = -\frac{qN_D}{\varepsilon}\int_0^{\varphi_C}d\varphi_C + \frac{qN_C}{\varepsilon} \times \int_0^{\varphi_C}\exp\left(\frac{q\varphi_C - q\varphi_f}{kT}\right)d\varphi_C \tag{21}$$

where $\varphi_f$ is the Fermi level potential, resulting in

$$E^2 = -\frac{2qN_D}{\varepsilon}\varphi_C + \frac{kTn_e}{\varepsilon} - \frac{kTN_C}{\varepsilon}\exp\left(\frac{-q\varphi_f}{kT}\right). \tag{22}$$

From (19), we can also obtain the following equation:

$$E = -\frac{d\varphi_C}{dx} = \frac{qN_D}{\varepsilon}x - \frac{q}{\varepsilon}\int_0^x n_e dx. \tag{23}$$

At two specific positions, the middle of the PPD $x = 0$ and the edge of depleted region $x = d$, the respective electrical field intensities are

$$E_{x=0} = 0 \tag{24}$$

$$E_{x=d} = qN_D d/\varepsilon - qN_e/\left(2\varepsilon S_{\text{PPD}}\right) \tag{25}$$

where $S_{\text{PPD}}$ is the area of the PPD. Substituting (24) and (25) with (22) results in

$$0 = -\frac{2qN_D}{\varepsilon}\varphi_C(0) + \frac{kTn_e(0)}{\varepsilon} - \frac{kTN_C}{\varepsilon}\exp\left(\frac{-q\varphi_f}{kT}\right) \tag{26}$$

$$\left(qN_D d/\varepsilon - qN_e/\left(2\varepsilon S_{\text{PPD}}\right)\right)^2 = -\frac{2qN_D}{\varepsilon}\varphi_C(d) + \frac{kTn_e(d)}{\varepsilon} - \frac{kTN_C}{\varepsilon}\exp\left(\frac{-q\varphi_f}{kT}\right). \tag{27}$$

Assuming the PPD has a square well and combining (26) and (27), $\Delta V_{C\text{nwell}}$ is approximately expressed as

$$\Delta V_{C\text{nwell}} \approx \varphi_C(0) - \varphi_C(d) = \frac{q}{2\varepsilon N_D}\left(N_D d - \frac{N_e}{2S_{\text{PPD}}}\right)^2 + \frac{kT}{q}\frac{\left(n_e(0) - n_e(d)\right)}{2N_D} \tag{28}$$

where the first term is much larger than the second term. Substituting (28) with (18) leads to

$$V_{\Delta C} \approx V_{\Delta C0} + q/\left(2\varepsilon N_D\right) \times \left(N_D d - N_e/\left(2S_{\text{PPD}}\right)\right)^2. \tag{29}$$

There is a parabolic relationship between $N_e$ and $V_{\Delta C}$ as shown in Fig. 8. It should be noted that the electron density

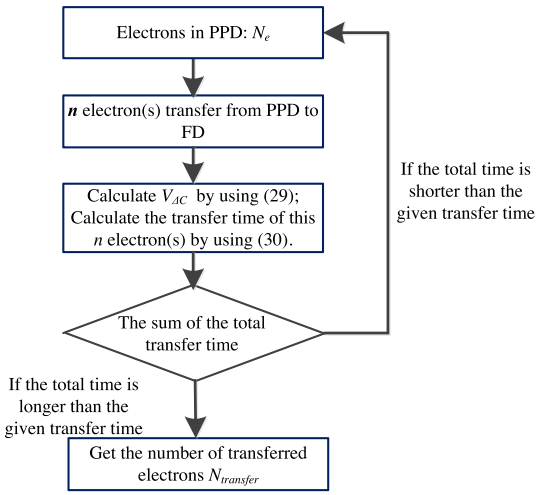


Fig. 9. Simulation flow of the level-2 model.

$N_e/V(n_e)$ is lower than the doping concentration $N_D$ in a working PPD.

Equation (29) is the corrected term for (8). Nevertheless, it is still difficult to achieve an analytical solution. An iterative method is used for the level-2 model simulation shown in Fig. 9, which requires the following equation, derived from (7), to calculate the transfer time of each electron:

$$t_i = qN_C V/I_0 \times \exp\left(qV_{\Delta C}/(kT)\right) \times \ln\left(N_e/(N_e - n)\right) \tag{30}$$

where $n$ represents the simulation step size.

An example of the simulation results is shown in Fig. 10, where the Richardson constant $A$ is 120 A/T$^2$cm$^2$, $S_A = 2\ \mu\text{m} \times 0.2\ \mu\text{m}$, $N_D = 3 \times 10^{15}$ cm$^{-3}$, $d = 0.25\ \mu$m, and $S_{\text{PPD}} = 4\ \mu\text{m} \times 4\ \mu$m. $N_{e0}$ and $N_{\text{transfer}}$ correspond to the exposure and the output, respectively. With a certain barrier height, as shown in Fig. 10(a), if the charge transfer time is not long enough, e.g., 100 or 300 ns, the transfer is incomplete and a nonlinear response is observed at the very beginning of the curve. Fig. 10(b) shows that the charge transfer speed becomes slower with a greater barrier height. The corresponding charge transfer inefficiency (CTI) curves are shown in Fig. 10(c), where the initial number of electrons is 10 000 e$^-$.

In [3], [11], and [12], the capacitor of the PPD $C_{\text{PPD}}$ is used to represent the charge holding capacity, and the potential variation is described by the differential form of $C_{\text{PPD}}$. In addition, we can obtain the expression of $C_{\text{PPD}}$ from (28). However, for [3], [11], and [12], the effect of Fermi level variation is neglected.

### D. Level-3 Model: Effect of FD Potential

In the level-1 and level-2 models, the effect of FD potential $\varphi_{\text{FD}}$ is neglected. In fact, $\varphi_{\text{FD}}$ decreases with an increase in number of transferred electrons. Electrons will transfer from the FD node back to the PPD through the thermionic emission process if $\varphi_{\text{FD}}$ is low enough.

Fig. 11 shows the potential profile of the TG tunnel and FD node, where $\varphi_{\text{pin}}$ is the lowest potential in region A and

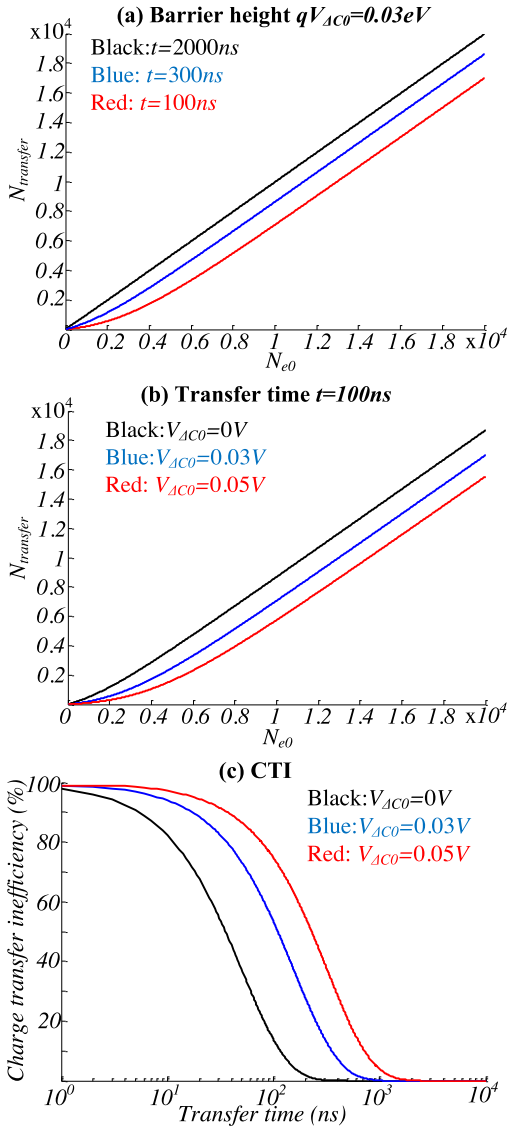


Fig. 10. Simulation results: photoresponse curves (a) with different transfer time, (b) with different barrier heights, and (c) CTI curves with different barrier heights.

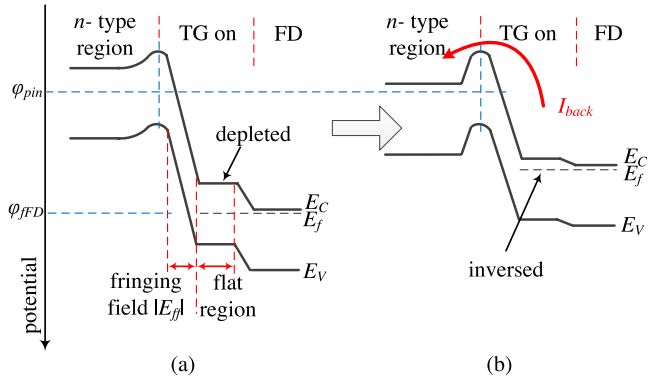


Fig. 11. TG tunnel and FD potential profile (a) for a small signal, the flat region is depleted and (b) for a large signal, the flat region is inversed.

is fixed with a certain voltage applied to the TG; $\varphi_{\text{fFD}}$ is the Fermi level potential of the TG tunnel and FD node; and $\varphi_{\text{frst}}$ is the value of $\varphi_{\text{fFD}}$ after the FD node reset.

1) If the number of transferred electrons from the PPD to the FD node is small, all the electrons are stored in the FD node and the TG tunnel is depleted. In this condition, $\varphi_{\mathrm{fFD}} - \varphi_{\mathrm{pin}}$ is high enough so that the emission current from the FD node back to the PPD can be neglected.
2) As the number of transferred electrons is increased, the potential of the FD and $\varphi_{\mathrm{fFD}}$ will become lower simultaneously. Finally, the TG tunnel becomes inversed; the emission current from the tunnel back to the PPD should be taken into consideration if the value of $\varphi_{\mathrm{fFD}} - \varphi_{\mathrm{pin}}$ is low enough.

In the level-3 model, the effect of the FD potential is considered. Emission current from the TG tunnel to the PPD is

$$I_{\mathrm{back}} = I_0 \exp(-q(\varphi_{\mathrm{fFD}} - \varphi_{\mathrm{pin}} + E_g/2q)/kT) \qquad (31)$$

where $E_g$ is the bandgap width, and we assume the charge transfer path from the FD node back to the PPD in region A is the same as the charge transfer path from the PPD to the FD node, so that $I_0$ need not to be corrected as it equals the value in (1). In the level-1 and level-2 models, we calculate the variation of the PPD Fermi level and conduction band, respectively. For the FD node, only the conduction band potential variation is considered, since the doping concentration of the FD node is much higher than that of the PPD, and the difference between the Fermi level and the conduction band is almost fixed, e.g., 0.05 eV. Thus, the relationship between the number of transferred electrons and the potential variation is

$$\Delta V_{\mathrm{FD}} = \varphi_{\mathrm{frst}} - \varphi_{\mathrm{fFD}} = q N_{\mathrm{transfer}} / (C_{\mathrm{FD}} + C_{\mathrm{TG}}) \qquad (32)$$

where $\Delta V_{\mathrm{FD}}$ is the variation of the FD potential, $C_{\mathrm{FD}}$ is the capacitance of the FD, and $C_{\mathrm{TG}}$ is the equivalent capacitance of the TG. From the famous $C$–$V$ curve of a MOS capacitor, we know that $C_{\mathrm{TG}}$ is not a constant. For small signal and large signal conditions, $C_{\mathrm{TG}}$ is approximately equal to zero and to the oxide capacitance, respectively. In order to simplify the discussion, we only consider the large signal condition, thus $C_{\mathrm{TG}}$ is equal to the oxide capacitance.

Fig. 12 shows the simulation flow of the level-3 model. An example of the simulation results is shown in Fig. 13, where $\varphi_{\mathrm{pin}} = 1.2$ V, $V_{\Delta C0} = 0.03$ V, $C_{\mathrm{FD}} = 1$ fF, $C_{\mathrm{TG}} = 1$ fF, and the other physical parameters are the same as the simulation of the level-2 model. As shown in Fig. 13(a), where $t = 1\ \mu s$, a higher reset voltage can improve the charge transfer capacity, and a small slope of the transfer curve $\alpha$ in the large signal region is observed. With a certain $N_{e0}$, the charge transfer process on the macrolevel will stop when $I_{\mathrm{PPD-FD}} = I_{\mathrm{back}}$. On the other hand, $I_{\mathrm{PPD-FD}}$ will become larger with an increase in the residual electrons in the PPD. The saturated output level ($N_{\mathrm{transfer}}$) will become slightly higher with the increase in exposure level ($N_{e0}$), since a larger $I_{\mathrm{back}}$ is needed for the balance, which also means a larger $N_{\mathrm{transfer}}$ is required. This is the reason for the presence of the small slope $\alpha$ in the saturation region. However, in the small signal region, the change in reset voltage has almost no effect on the charge transfer efficiency. The incomplete charge

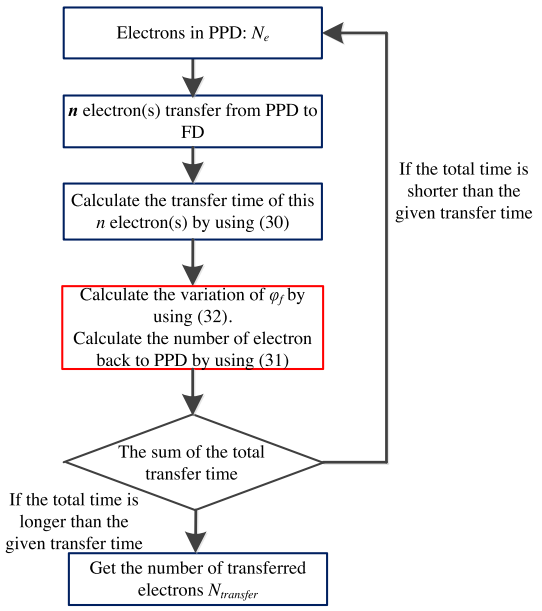


Fig. 12. Simulation flow of the level-3 model.

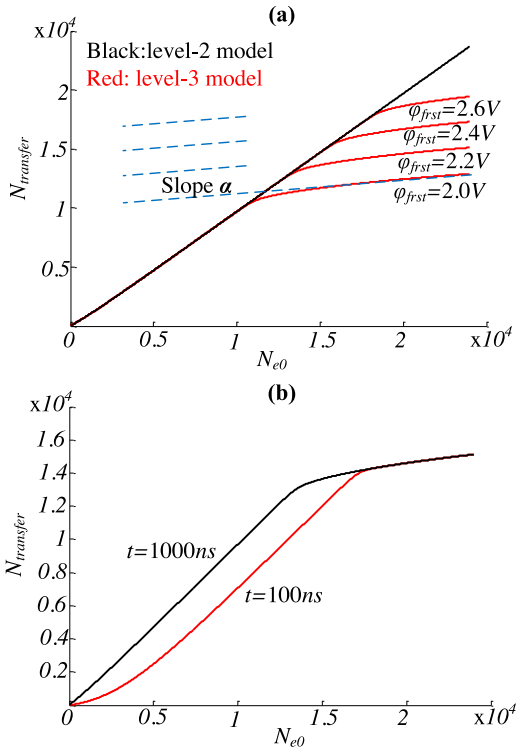


Fig. 13. Simulation results (a) level-2 versus level-3 model and (b) with different transfer time.

transfer case is shown in Fig. 13(b). The difference between the charge transfer curves with a different $t$ becomes narrow in the saturation region, meaning that they will finally intersect with each other.

The level-3 model describes the bidirectional emission process. Both the FWC of the PPD and the FD node will affect the slope $\alpha$ in the saturation region, since both of them affect the balance between $I_{\mathrm{PPD-FD}}$ and $I_{\mathrm{back}}$. For example,

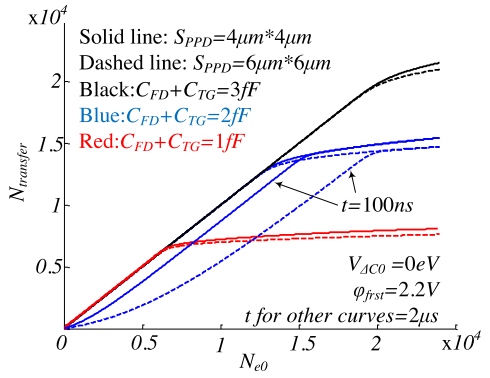


Fig. 14. Simulation results: slope $\alpha$ in the saturation region.

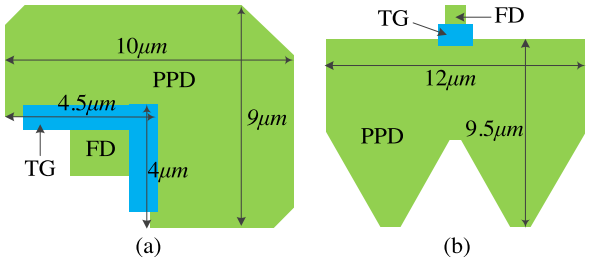


Fig. 15. (a) Test pixel in chip A. (b) Test pixel in chip B.

if the FWC of the PPD is fixed, we can achieve a larger $\alpha$ with a larger $C_{\mathrm{FD}}$. Conversely, if $C_{\mathrm{FD}}$ is fixed, we can reach a larger $\alpha$ with a smaller FWC of the PPD, as shown in Fig. 14. Furthermore, the area of the PPD will affect the charge transfer efficiency without even considering the thermal diffusion inside the PPD.

## III. Measurement Results

In this section, some measurement results obtained from two different test chips will be shown. Chip A was fabricated in a technology for which we could adjust the pixel implants. Chip B was fabricated in a standard 180-nm CIS process, and the source follower (SF) and row select transistor (SEL) were implemented by pMOS transistors. Both of the test pixels have a large area but also a special design for a built-in electric field inside the PPD, as shown in Fig. 15. The performance of the W-shaped pixel in chip B has been published in [1].

### A. Measurement Results of Chip A

The test pixel in chip A is L-shaped as shown in Fig. 15(a), and $C_{\mathrm{FD}}$ is ~8 fF. We changed the doping concentration for the TG by several special $p$-type implants, and two pixels with a high barrier height on the same wafer were selected for this discussion. In chip A, all the transistors in the pixel were implemented by nMOS, the voltage applied to the TG was 3.3 V, the reset voltage of the FD node was ~2.7 V.

Fig. 16 shows the measurement results, which correspond to the simulation results in Fig. 10. In the linear response region, we consider all the electrons to be transferred from the PPD to the FD node if $t$ is long enough. Then, $N_{e0}$ is obtained by multiplying the exposure by the average sensitivity

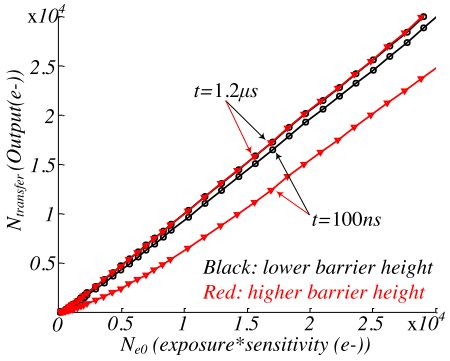


Fig. 16. Measurement results of chip A: photoresponse curves with different barrier heights.

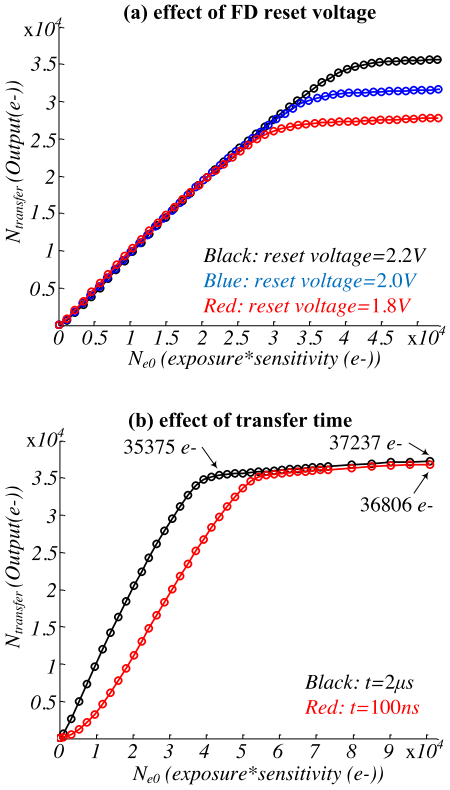


Fig. 17. Measurement results of chip B (a) with different reset voltages of the FD and (b) with different transfer times.

with longer $t$ (1.2 $\mu$s for Fig. 16 and 2 $\mu$s for Fig. 17). The black curves and red curves correspond to the pixels with lower barrier height and greater barrier height, respectively. As the model predicts, the charge transfer process has a strong correlation with barrier height. Normally, a lower doping concentration in the tunnel region improves the charge transfer performance, but the FWC of the PPD will decrease because of the feedforward effect [3].

Since the pixel transistors in chip A were implemented by nMOS, the readout of a large signal is limited by the SF. In order to observe the large signal region of the response curves, the measurement results obtained from the pixel with the pMOS SF and SEL will be shown in Section III-B.

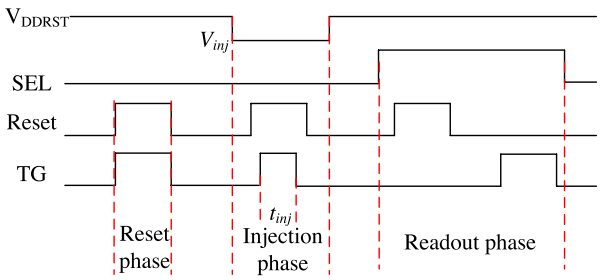


Fig. 18. Timing for pinning voltage measurement.

### B. Measurement Results of Chip B

The test pixel in chip B is W-shaped as shown in Fig. 15(b), where $C_{\mathrm{FD}}$ is ~4 fF, the width of the TG is 0.9 $\mu$m, and the FWC is limited by the FD node rather than the PPD. Fig. 17 shows the measurement results of the test pixel in chip B, where Fig. 17(a) and (b) corresponds to the simulation results in Fig. 13(a) and (b), respectively.

As shown in Fig. 17(a), the reset voltage of the FD node is varied, and the transfer time is fixed at 2 $\mu s$. In the small signal region, the variation of the FD reset voltage has almost no effect on the charge transfer. In fact, a small difference between the various curves is observed due to the nonlinearity of the SF. In the large signal region, the curve with the lowest FD reset voltage 1.8 V enters saturation first, and the curve with the highest FD reset voltage 2.2 V has the largest output range. The improvement in the output range ($e^-$) is equal to $C_{\mathrm{FD}}\Delta V_{\mathrm{rst}}/q$, where $\Delta V_{\mathrm{rst}}$ is the reset voltage difference.

As shown in Fig. 17(b), the transfer time is varied, and the reset voltage of the FD is fixed at 2.2 V. The difference between the two curves with a different $t$ becomes narrow in the saturation region. Yet a small difference still exists between them which originates from the thermal diffusion process inside the PPD; this is not considered in our model. In addition, a small slope is observed in the saturation region as the model predicts.

## IV. Model Extension

### A. Explanation for the Pinning Voltage Measurement

The method for measuring the pinning voltage was first reported in [22], and later explained in [23]. The measurement timing is shown in Fig. 18. During the injection phase, the TG and the reset transistor are open, and the number of electrons injected from the FD node to the PPD is controlled by varying $V_{\mathrm{inj}}$, where $V_{\mathrm{inj}}$ is the voltage of $V_{\mathrm{DDRST}}$ during the injection phase.

We use the level-3 model to describe the charge injection process during the injection phase. The only difference is that $\varphi_{\mathrm{fFD}}$ is fixed, and $\varphi_{\mathrm{fFD}} = V_{\mathrm{inj}}$. Fig. 19 shows the simulation results for the method used to measure the pinning voltage, where $\varphi_{\mathrm{pin}} = 1.2$ V, $V_{\Delta C0} = 0.03$ V, and all other physical parameters are the same as the simulation of the level-2 model. In the transition region, the shape of the curve has a correlation with injection time $t_{\mathrm{ing}}$; similar measurement results can be found in [23]. When the PPD is empty, $V_{\Delta C} = 0.14$ V$+V_{\Delta C0}$, which can be extracted from (29) and Fig. 8. Then, we can obtain the potential inside the PPD $\varphi_{\mathrm{ppd}}$, and $\varphi_{\mathrm{ppd}} = \varphi_{\mathrm{pin}} + V_{\Delta C} = 1.37$ V.

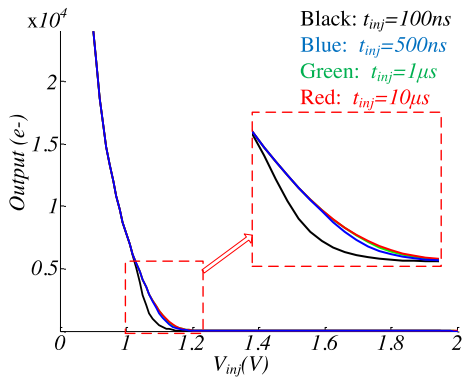


Fig. 19. Simulation results for the pinning voltage.

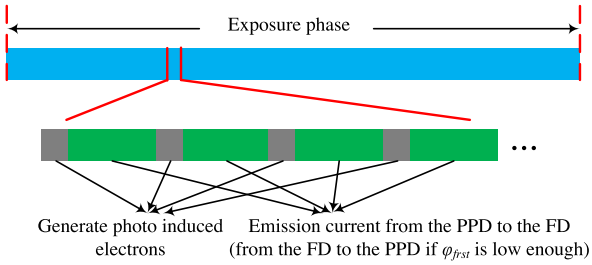


Fig. 20. Simulation method for the feedforward effect.

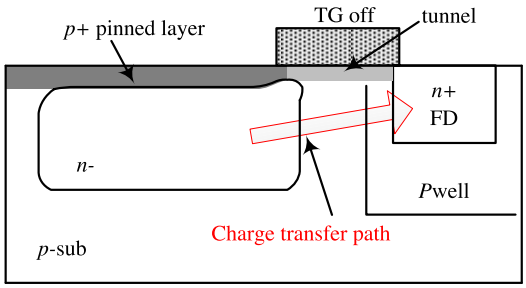


Fig. 21. Charge transfer path when the TG is OFF.

### B. Feedforward Effect During Exposure Phase

The feedforward effect, which is explained by the thermionic emission theory, is reported in [3]. This effect influences the FWC of the PPD. During the exposure phase, both the photogenerated current inside the PPD and the emission current from the PPD to the FD node exist if the barrier height is not high enough. Therefore, these two processes should be simulated simultaneously during the exposure phase; the simulation method is shown in Fig. 20. The entire exposure phase consists of $m$ interval periods. The photoinduced electrons generate at the very beginning of each interval period, and the emission current is simulated by the level-2 model during the rest of this period (using the level-3 model if $\varphi_{\mathrm{frst}}$ is very low).

Fig. 21 shows the charge transfer path when the TG is OFF, and the position depends on the doping profile between the

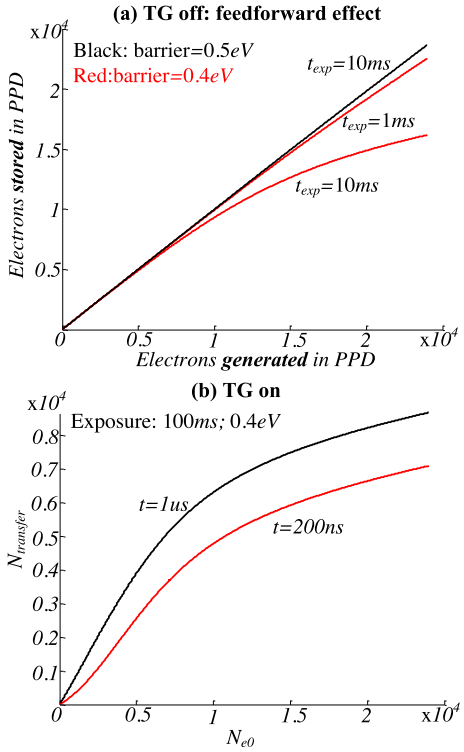


Fig. 22. Simulation results. (a) Feedforward effect. (b) Photoresponse curves limited by the FWC of the PPD.

PPD and the FD node. In the simulation for the feedforward effect, $m = 1000$, and the physical parameters are the same as in the simulation of the level-2 model. As shown in Fig. 22(a), a greater barrier height and shorter exposure time $t_{\text{exp}}$ will increase the equivalent FWC of the PPD during the exposure phase. The same conclusion can be found in [3]. Fig. 22(b) shows the photoresponse curves limited by the FWC of the PPD, which is very different from the curves limited by the FWC of the FD node as shown in Fig. 13(b). The difference between the two curves with a different $t$ does not become smaller in the large signal region. A similar measurement result can be found in [5].

## V. Conclusion

Based on the thermionic emission theory, we established a charge transfer model to describe the charge transfer process between the PPD and the FD node. The model is suitable for small pixels and large pixels with a special design for an extra built-in electric field.

For a small signal, both a short charge transfer time and a high potential barrier on the charge transfer path will result in a nonlinear photoresponse, and the reset voltage of the FD has almost no effect on the charge transfer, the measurement results of which are consistent with the model prediction. For a large signal, both the model prediction and the measurement results show that the output level is limited by the reset voltage of the FD if the FWC is limited by the FD node, and a small slope in the saturation region of the photoresponse curve is observed. However, the level-3 model predicts that the photoresponse curves with a different transfer time will finally intersect with each other, which was not observed in the measurement results. In fact, a small difference still exists between them which originates from the thermal diffusion process inside the PPD; this is not considered in our model.

The model also predicts that the width of the TG, the capacitance of the FD node, the equivalent capacitance of the TG, and even the area ratio between the PPD and the FD node, which can be controlled by the pixel designer, will affect the charge transfer efficiency. Furthermore, the model can be extended to explain the pinning voltage measurement method and the feedforward effect. We hope this model can help the readers to understand more about the charge transfer process between the PPD and the FD node, thus allowing better pixel design.

## Acknowledgment

The authors would like to thank Y. Xu and X. Ge for providing test chip B and helping with the measurement.

## References

[1] Y. Xu and A. J. P. Theuwissen, "Image lag analysis and photodiode shape optimization of 4T CMOS pixels," in *Proc. Int. Image Sensor Workshop*, Jun. 2013, pp. 153–157.
[2] J. P. Carrère, S. Place, J. P. Oddou, D. Benoit, and F. Roy, "CMOS image sensor: Process impact on dark current," in *Proc. IEEE Int. Rel. Phys. Symp.*, 2014, pp. 3C.1.1–3C.1.6.
[3] M. Sarkar, B. Büttgen, and A. J. P. Theuwissen, "Feedforward effect in standard CMOS pinned photodiodes," *IEEE Trans. Electron Devices*, vol. 60, no. 3, pp. 1154–1161, Mar. 2013.
[4] Y. Li, B. Li, J. Xu, Z. Gao, C. Xu, and Y. Sun, "Charge transfer efficiency improvement of a 4-T pixel by the optimization of electrical potential distribution under the transfer gate," *J. Semicond.*, vol. 33, no. 12, p. 124004, Dec. 2012.
[5] Z. Cao *et al.*, "Process techniques of charge transfer time reduction for high speed CMOS image sensors," *J. Semicond.*, vol. 35, no. 11, p. 114010, Nov. 2014.
[6] H. Mutoh, "3-D optical and electrical simulation for CMOS image sensors," *IEEE Trans. Electron Devices*, vol. 50, no. 1, pp. 19–25, Jan. 2003.
[7] J. Michelot *et al.*, "Back illuminated vertically pinned photodiode with in depth charge storage," in *Proc. Int. Image Sensor Workshop*, Jun. 2011, pp. 24–27.
[8] B. Shin, S. Park, and H. Shin, "The effect of photodiode shape on charge transfer in CMOS image sensors," *Solid-State Electron.*, vol. 54, no. 11, pp. 1416–1420, Nov. 2010.
[9] A. J. P. Theuwissen, *Solid-State Imaging With Charge Coupled Devices*. Boston, MA, USA: Kluwer, 1995, pp. 27–35.
[10] E. R. Fossum and D. B. Hondongwa, "A review of the pinned photodiode for CCD and CMOS image sensors," *IEEE J. Electron Devices Soc.*, vol. 2, no. 3, pp. 33–43, May 2014.
[11] N. Teranishi, A. Kohono, Y. Ishihara, E. Oda, and K. Arai, "No image lag photodiode structure in the interline CCD image sensor," in *Proc. IEDM*, Dec. 1982, pp. 324–327.
[12] E. R. Fossum, "Charge transfer noise and lag in CMOS active pixel sensors," in *Proc. IEEE Workshop Charge-Coupled Devices Adv. Image Sensors*, May 2003, pp. 149–154.
[13] S. M. Sze, *Physics of Semiconductors*, 2nd ed. New York, NY, USA: Wiley, 1981, pp. 255–258.
[14] I. Inoue, N. Tanaka, H. Yamashita, T. Yamaguchi, H. Ishiwata, and H. Ihara, "Low leakage current and low operating voltage buried photodiode for a CMOS imager," *IEEE Trans. Electron Devices*, vol. 50, no. 1, pp. 43–47, Jan. 2003.
[15] J. Yu, B. Li, P. Yu, J. Xu, and M. Cun, "Two-dimensional pixel image lag simulation and optimization in a 4-T CMOS image sensor," *J. Semicond.*, vol. 31, no. 9, p. 094011, Sep. 2010.
[16] B. Mheen, Y.-J. Song, and A. J. P. Theuwissen, "Negative offset operation of four-transistor CMOS image pixels for increased well capacity and suppressed dark current," *IEEE Electron Device Lett.*, vol. 29, no. 4, pp. 347–349, Apr. 2008.

[17] Z. Cao, Y. Zhou, Q. Li, L. Liu, and N. Wu, "Design of pixel for high speed CMOS image sensors," in *Proc. Int. Image Sensor Workshop*, Jun. 2013, pp. 229–232.
[18] L. Bonjour, N. Blanc, and M. Kayal, "Experimental analysis of lag sources in pinned photodiodes," *IEEE Electron Device Lett.*, vol. 33, no. 12, pp. 1735–1737, Dec. 2012.
[19] L. Han, S. Yao, J. Xu, C. Xu, and Z. Gao, "Analysis of incomplete charge transfer effects in a CMOS image sensor," *J. Semicond.*, vol. 34, no. 5, p. 054009, May 2013.
[20] K. Yasutomi, S. Itoh, S. Kawahito, and T. Tamura, "Two-stage charge transfer pixel using pinned diodes for low-noise global shutter imaging," in *Proc. Int. Image Sensor Workshop*, Jun. 2009, pp. 333–336.
[21] B. Van Zeghbroeck, *Principles of Semiconductor Devices*. Boulder, CO, USA: Univ. Colorado, 2004, chs. 2–7. [Online]. Available: http://ece-www.colorado.edu/~bart/book/
[22] J. Tan, B. Büttgen, and A. J. P. Theuwissen, "Analyzing the radiation degradation of 4-transistor deep submicron technology CMOS image sensors," *IEEE Sensors J.*, vol. 12, no. 6, pp. 2278–2286, Jun. 2012.
[23] V. Goiffon *et al.*, "Pixel level characterization of pinned photodiode and transfer gate physical parameters in CMOS image sensors," *IEEE J. Electron Devices Soc.*, vol. 2, no. 4, pp. 65–76, Jul. 2014.

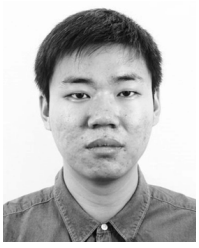

**Liqiang Han** (S'13) received the B.E. degree from the School of Electronic Information Engineering, Tianjin University, Tianjin, China, in 2010, where he is currently pursuing the Ph.D. degree in microelectronics and solid electronics.

He has been a Visiting Student with the Electronic Instrumentation Laboratory, Delft University of Technology, Delft, The Netherlands, since Oct. 2014.

**Suying Yao** (M'11) received the B.E. degree from Tianjin University, Tianjin, China, in 1970.

She is currently a Professor and Ph.D. Candidate Supervisor with the School of Electronic Information and Engineering, Tianjin University, and the Director of the Tianjin University Application Specific Integrated Circuit (ASIC) Design Center. Her current research interests include CMOS image sensors, ASICs, and device modeling.

**Albert J. P. Theuwissen** (M'82–SM'95–F'02) received the Ph.D. degree in electrical engineering from the Catholic University of Leuven, Leuven, Belgium, in 1983.

He started Harvest Imaging, Bree, Belgium, where he focuses on consulting, training, and teaching in solid-state imaging technology, after he left DALSA. He is currently a part-time Professor with the Delft University of Technology, Delft, The Netherlands.